Research Article

Cryo-EM exposes diverse polymorphism in IAPP mutants to guide the rational design of peptide-based therapeutics

Saik Ann Ooi [1], Dylan Valli [2], Mikołaj I. Kuska [2], Helena Marí [3,4], Himanshu Chaudhary [2], Weixiao Yuan Wahlgren [1], Sebastian Westenhoff [5], Alesia A. Tietze [1], Anna Novials [3,4], Joan-Marc Servitja [3,4], and Michał Maj [2,*]

*1 - **Department of Chemistry and Molecular Biology,** Medicinaregatan 7B, Gothenburg 413 90, Sweden*
*2 - **Department of Chemistry – Ångström Laboratory,** Uppsala University, Box 523, Uppsala 751 20, Sweden*
*3 - **Pathogenesis and Prevention of Diabetes Group,** Institut d'Investigacions Biomèdiques August Pi i Sunyer (IDIBAPS), Barcelona Spain*
*4 - **Centro de Investigación Biomédica en Red de Diabetes y Enfermedades Metabólicas Asociadas (CIBERDEM),** Spain*
*5 - **Department of Chemistry - BMC,** Biochemistry, Uppsala University, Uppsala 75123, Sweden*

***Correspondence to Michał Maj:** michal.maj@kemi.uu.se (M. Maj)*
https://doi.org/10.1016/j.jmb.2025.169405
Edited by: Gabriel Lander

Abstract

In the pursuit of potential therapeutic agents for type 2 diabetes, non-amyloidogenic forms of the human Islet Amyloid Polypeptide (hIAPP) containing site-specific mutations are of significant interest. In the present study, we dissect the three proline mutations present in the core region of the non-amyloidogenic rat IAPP into single-point mutations at A25P, S28P, and S29P sites. We apply high-resolution cryo-electron microscopy and solve the structures of 6 polymorphs formed by these mutants, revealing the peptide's self-assembly patterns and identifying critical interactions that reinforce these structures in the presence of the β-sheet breaker. A unique trimeric aggregate with C3 symmetry was identified in the A25P mutant, which we resolved with a 3.05 Å resolution, while asymmetric trimeric assemblies were observed in the other mutants. Guided by the high-resolution structural models of A25P and S28P fibrils obtained in our study, we successfully designed novel non-amyloidogenic mutants of IAPP with potential therapeutic value. Our findings demonstrate the immense potential of structure-based approaches in developing effective therapeutics against amyloid diseases.

Introduction

Amyloid diseases show a profound dualism in biology: proteins that support life can also, through a process of misfolding, become agents of disease.[1] In amyloidosis, this misfolding leads to the formation of fibrils that accumulate in organs and tissues. Such behavior of amyloid proteins thus represents a unique challenge, demanding a deeper understanding of the mechanisms of their self-assembly and innovative approaches in treatment.

The human islet amyloid polypeptide (hIAPP), a peptide hormone co-secreted with insulin, is a noteworthy example in type 2 diabetes (T2D). Normally involved in key physiological processes, such as regulating satiety and glucose homeostasis, hIAPP can aggregate into amyloid plaques under pathological conditions.[2] Amyloid deposition is observed in over 90 % of all patients with T2D.[3] These aggregates disrupt normal cellular functions, leading to the impaired insulin production characteristic of T2D.[4–6] Although the precise

mechanisms of amyloid formation are not yet fully understood, factors such as hyperglycemia, chronic β-cell stress, proinflammatory signaling, and cross-seeding by other amyloidogenic proteins have been implicated in promoting hIAPP misfolding and aggregation.[7] This type of amyloid deposition is not isolated to T2D but is a common pathological feature in various other protein misfolding diseases, such as Alzheimer's and Parkinson's disease.[8]

The important physiological functions of IAPP, particularly in regulating blood glucose levels, highlight its potential as a therapeutic agent in T2D.[9] However, the wild-type (WT) peptide cannot be directly used due to its propensity to rapidly assemble into amyloid fibrils.[10] Therefore, non-amyloidogenic forms of IAPP that retain their activity are used in place of the WT peptide.[11,12] Rat islet amyloid polypeptide (rIAPP) is known to not aggregate under physiological conditions, thus not contributing to the development of diabetes in rodents.[13,14] rIAPP differs from hIAPP in only a few amino acids, including three prolines in the so-called amyloidogenic core (Fig. 1a). Pramlintide, an IAPP analog, was developed by incorporating these proline residues at positions Ala25, Ser28, and Ser29 from the rat sequence into the human variant.[15] Pramlintide exhibits greater solubility than hIAPP and has been adopted as an adjunctive treatment for T2D. However, the need for two separate injections – one for insulin and one for Pramlintide – is problematic, as Pramlintide needs to be formulated at a lower pH than insulin.[16] Consequently, the search for improved formulation is still on-going, with new promising IAPP analogs undergoing clinical trials.[17]

The structure of amyloid fibrils formed by hIAPP provides essential insights into the interactions that stabilize their architecture. With recent advancements, it has become possible to extract three-dimensional structures from heterogeneous mixtures of amyloid fibril polymorphs using helical reconstruction of particles captured through cryo-electron microscopy (cryo-EM).[18–21] To date, several structures of WT hIAPP have been determined for both *in vitro* and *ex vivo* seeded samples.[22–27].

Building upon this, there is a great potential to guide the creation of novel non-amyloidogenic IAPP variants with therapeutic value. These detailed structures allow for the identification of potential sites where the introduction of β-sheet breakers, like proline residues,[28] could disrupt fibril stability. Mutation studies utilizing proline residues have been reported in the literature and the results highlight significant differences in the inhibition of amyloid aggregation based on the specific site of proline mutation, as evidenced by Thioflavin T (ThT) fluorescence assays.[29–31] However, it must be noted that even the incorporation of double proline mutations directly into the amyloidogenic core does not completely prevent peptide aggregation.[30] This observation suggests that although the core region is the most critical for fibrillation, interactions outside this motif may also play a significant role in overall fibril stability. Amyloid aggregation is known to proceed through the formation of oligomers and pre-fibrillar intermediates.[32–34] The exact structure of these species is unknown and they are difficult to solve with the existing structural biology and computational methods, including generative AI models. This further complicates predicting mutation sites that disfavor aggregation, which hinders the strategic design of peptide-based therapeutics.

To deliver critical information that could aid the rational design of active non-amyloidogenic forms of IAPP, we investigate the importance of individual residues in the amyloidogenic core region of IAPP in the process of fibril formation. Our approach involves introducing proline mutations, drawing inspiration from the structural characteristics of Pramlintide and rat IAPP. Proline is recognized for its ability to disrupt β-sheets by interfering with the hydrogen bonding (H-bonding) interactions,[28] thus altering the structural integrity and morphology of fibrils. However, the precise structural changes induced by proline residues have never been resolved with high-resolution.

To elucidate the effects of incorporating proline at specific positions, we performed individual proline mutations on the WT hIAPP sequence, specifically yielding A25P, S28P, and S29P mutants of hIAPP. By applying high-resolution cryo-EM, we identified that each of these proline mutants assembles into fibrils encompassing multiple distinct polymorphic structures. Through helical reconstruction techniques, we resolved the residue-level structures of six distinct polymorphs derived from the proline mutants. These polymorphs exhibit significant deviations from structures of WT hIAPP previously described in the literature. By combining the structural information from both the WT and the mutant structures, we successfully perform the first rational structure-based design of a novel non-amyloidogenic hIAPP mutant with therapeutic potential.

Results and discussion

Kinetics of fibril formation

To monitor the aggregation kinetics of WT hIAPP and its proline mutants, we employed ThT fluorescence assays, which is a standard method for monitoring amyloid fibril formation.[36] The results are presented in Fig. 1a. The peptide concentration was maintained at 100 μM and HEPES buffer at pH 7.4 was used in all experiments. HEPES was selected as it ensures reproducible aggregation kinetics and minimizes fibril clustering, a property that also yields superior sample quality for cryo-EM analysis.[37] The resulting curves consistently display a sigmoidal shape, indicative of a nucleation mechanism. An evident lag phase was observed,

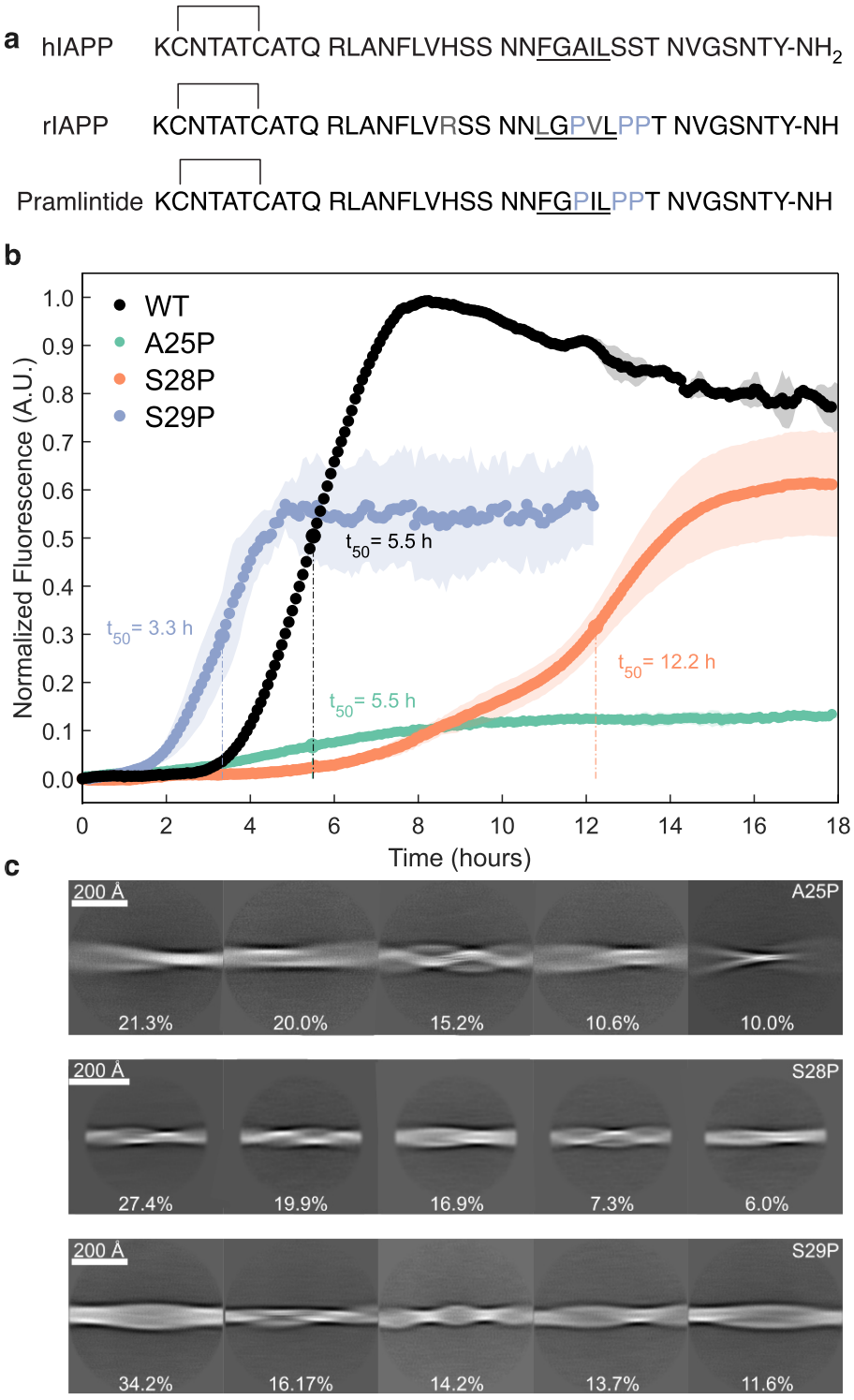

Fig. 1. Proline mutations in the hIAPP core alter aggregation kinetics and fibril polymorphism. (a) Sequences of hIAPP, non-amyloidogenic rIAPP, and the therapeutic analog Pramlintide. The location of the amyloidogenic core (FGAIL) is underlined and substitutions relative to the WT hIAPP sequence are shown in blue. (b) Aggregation kinetics of WT hIAPP and proline mutants in HEPES buffer pH 7.4. Among the mutants, S29P has the fastest aggregation kinetics followed by A25P and S28P. ThT fluorescence intensity is plotted over time and each experiment was performed in triplicates. The data is normalized to the maximum intensity of the WT peptide. Standard deviation at each time point is represented by shaded areas (c) Representative cryo-EM 2D class averages of the main twisted polymorphs found for each mutant. The results of bi-hierarchical classification of filaments[35] which includes examples of non–helical 2D classes are given in the SI.

suggesting that the aggregation process initiates from the monomeric state in all measured samples.

To quantify the aggregation rate, we evaluated two parameters: the duration of the lag phase and the t_{50}. The latter is defined as the time required to achieve 50 % of the final fluorescence intensity and is an efficient way of quantifying the length of the elongation phase. Both the t_{50} parameter and the lag phase were determined using nonlinear regression by fitting the kinetic curves to a sigmoidal function, as described in the literature.[38] Under the experimental conditions used, the WT peptide exhibited a lag phase of 4.6 $\pm$ 0.1 h and a t_{50} of 5.50 h with perfect agreement across triplicates. These values are in a similar range to the ones reported before;[30] however it is important to note that our experiments were conducted at concentrations approximately six times greater and that the aggregation rates do not have a linear relationship with concentration.[39] It is generally known that the aggregation process is dependent on many factors and has a certain degree of randomness due to the stochastic nature of the nucleation process.[40,41] Despite this, we detected minimal variation in aggregation times across repeated measurements at this relatively high concentration.

Among the proline mutants, the aggregation of S29P appears to be not inhibited by the mutation. Despite an overall decrease in fluorescence intensity, the lag phase appears to be about twice as short and amounts to 2.1 $\pm$ 0.2 h while the t_{50} is observed at 3.5 $\pm$ 0.3 h. The lack of noticeable change in the aggregation kinetics of S29P is in some way expected as the mutation is prevalent,[42] also among those animals that readily develop diabetes, which is not the case for A25P and S28P mutants we discuss next.

The aggregation kinetics of the A25P mutant differ from those of both the WT and S29P peptides. The aggregation process is inhibited, resulting in a final fluorescence intensity that reaches only about 20 % of the maximum observed for WT hIAPP. However, the lag phase and the t_{50} are not significantly affected. The lag phase was estimated to be 1.5 $\pm$ 0.4 h while the elongation phase was 5.6 $\pm$ 0.1 h. The aggregation kinetics show a strong dependence on peptide concentration; for comparison, aggregation of A25P mutant at a reduced concentration of 25 μM (Fig. S2) increases the t_{50} to approximately 16 h. Elevated salt concentrations, however, accelerate the aggregation process (Fig. S3).

The S28P mutant exhibits the slowest aggregation kinetics among all studied peptides. Its kinetics are characterized by an extended lag phase, significantly slower elongation, and reduced fluorescence intensity. The lag phase was estimated to be 7.5 $\pm$ 0.2 h, and the t_{50} was determined to be 12.2 $\pm$ 0.2 h. Furthermore, the S28P mutant shows the strongest dependence of aggregation kinetics on the initial peptide concentration, with previous studies reporting that it is completely non-amyloidogenic at concentrations of 16 μM or lower.[30] Similar to other IAPP peptides, high salt concentrations accelerate the aggregation process of the S28P mutant.

It is important to note that while ThT fluorescence is a widely accepted indicator of amyloid formation, the binding affinity of ThT can be somewhat influenced by fibril morphology. In our related studies, we observed that flat fibrils bind ThT more efficiently than other fibril polymorphs, though the effect is relatively minor.[43] Nevertheless, ThT fluorescence remains a reliable qualitative measure of the aggregation process; however, for a more quantitative analysis, techniques such Western blotting may provide more accurate estimates.

Interestingly, despite the two mutated serine residues being just a position apart, they display markedly different kinetics. Moreover, it appears that mere proximity to the amyloidogenic core (FGAIL region) does not solely dictate this behavior. To shed light on the structural factors driving the observed changes in the aggregation rates, we apply cryo-EM to inspect the residue-level structures of amyloid fibrils formed by the studied mutants.

Cryo-EM analysis of fibril polymorphism

For each of the studied mutants, we collected several thousands of micrographs to capture the diverse array of polymorphic structures. Details of data acquisition, image processing and reconstruction are presented in Table 1. The workflow schematic is also shown in Fig. S6. We used a modified version of Topaz[44] for automatic filament picking and RELION4 for subsequent 2D classification.[45,46] We excluded flat fibrils lacking helical symmetry, while the helically twisted fibrils were grouped into the most abundant class averages for further analyses. The bi-hierchical filament clustering algorithm[35] implemented in RELION was used to separate 2D class averages and the clustering results are presented in Fig. S7. The most representative 2D class averages of helical filaments for each mutant are depicted in Fig. 1b. For the A25P mutant, flat fibrils represented 69 % of all selected particles, with the remaining 31 % exhibiting helical twists. In contrast, the S29P mutant had a higher proportion of twisted fibrils, at 85 %. The S28P mutant demonstrated the highest incidence of helical filaments, with nearly all particles exhibiting helical symmetry. In the analysis of the A25P mutant, we observed significant diversity in particle appearance, with 2D class averages revealing significantly different fibril morphology, crossover distances, and diameters. The observed cross-over distances were all within the range of approximately 300–600 Å and the diameters ranged from 50–80 Å, which is typical for previously reported hIAPP poly-

Table 1 Data collection and refinement parameters.

	A25P-P1 (EMDB-18441) (PDB QJ1)	S28P-P1 (EMDB-19353) (PDB RM8)	S28P-P2 (EMDB-19354) (PDB RM9)	S29P-P1 (EMDB-18671) (PDB QVP)	S29P-P2 (EMDB-18672) (PDB QVQ)	S29P-P3 (EMDB-18673) (PDB QVR)
Data collection and processing						
Magnification	105 000	165 000	165 000	165 000	165 000	165 000
Voltage (kV)	300	300	300	300	300	300
Electron exposure (e^{-}/Å^2)	23	44	44	58	58	58
Defocus range (μm)	−0.6 to −2	−1.2 to −2.4	−1.2 to −2.4	−0.6 to −2.4	−0.6 to −2.4	−0.6 to −2.4
Pixel size (Å)	0.856 (recalibrated 0.828)	0.704	0.704	0.821	0.821	0.821
Symmetry imposed	C3	C1	C1	C2	C1	C1
Twist (°)	−2.13	−2.09	−1.76	−3.28	−3.61	−1.98
Rise (Å)	4.85	4.78	4.73	4.83	4.76	4.75
Initial particles images (No.)	43444	53814	83723	30742	30742	49405
Final particles images (No.)	9726	6613	4193	4930	4442	6374
Map resolution (Å)	3.05	3.00	3.6	3.75	3.44	3.25
Refinement						
Initial model used (PDB code)	De novo	De novo	De novo	De novo	De novo	De novo
Model resolution (Å)	3.05	3.00	3.6	3.75	3.44	3.25
FSC threshold	0.143	0.143	0.143	0.143	0.143	0.143
Map sharpening B factor (Å^2)	−66.3	−76.2	−83.9	−77.4	−74.6	−43.2
Model composition						
Non–hydrogen atoms	3990	2035	3160	2260	2545	2255
Proteins residues	540	270	425	300	345	305
Ligands	15	10	15	10	15	10
B factors (Å^2)						
Protein	56.04	90.61	135.05	74.93	55.45	80.29
Ligand	59.86	99.79	123.1	72.07	57.66	87.02
R.m.s.d.						
Bond lengths (Å)	0.004	0.008	0.006	0.005	0.005	0.005
Bond angles (°)	0.961	1.208	1.219	0.951	1.006	0.975
Validation						
MolProbity score	1.27	1.64	1.31	1.32	0.95	1.33
Clashscore	5.06	13.45	5.75	5.90	1.85	5.98
Rotamers outlier (%)	0	0	0	0	0	0
EMRinger score	1.57	1.12	3.73	1.6	3.74	3.56
Q-Score (%)	0.56	0.41	0.56	0.59	0.57	0.65
Ramachandran plot						
Favored (%)	100	100	100	100	100	100
Allowed (%)	0	0	0	0	0	0
Disallowed (%)	0	0	0	0	0	0

morphs. This diversity suggests a range of unique fibril architectures, with no particles resembling any of the structures previously observed for the WT hIAPP. The S28P mutant shows less variability, as the majority of particles share similar diameters and the difference in twist and crossover distances are not as pronounced. The S29P mutant was characterized by the longest crossover distances among the most prevalent classes.

In subsequent stages, we carried out additional 2D and 3D classifications for each particle group with the goal of isolating particles suitable for high-resolution 3D reconstruction. Despite these efforts, not all polymorphic structures could be solved, a challenge attributed to factors such as suboptimal particle quality, significant heterogeneity within class averages, or excessive crossover distances. This outcome aligns with previous findings that high-quality appearances in class averages do not guarantee successful reconstruction.[27] Ultimately, for the A25P mutant, the most twisted polymorph was resolved, representing approximately one-third of all twisted particles identified in the micrographs. In the case of the S28P mutant, two resolved structures accounted for nearly 70 % of all identified twisted fibrils. For the S29P mutant, we have resolved three polymorphs from the 2D class averages, corresponding to about 54 % of all the examined helical segments.

Helical reconstruction and 3D refinements

hIAPP-A25P-P1 (PDB 8QJ1). The first and only polymorph of hIAPP-A25P mutant was resolved to a 3.05 Å resolution. It exhibits a fibrillar structure comprising three filaments organized in C3 rotational symmetry (Fig. 2a-b). Although high symmetry in multi-filament assemblies is not uncommon in certain amyloid fibrils, including some prion proteins,[21,47,48] this highly symmetric structure had not been observed for IAPP before. Typically, the full amino acid sequence is challenging to resolve in IAPP due to the high flexibility of the flanking regions at the N-terminus. However, for each chain in A25P-P1, we observe clear density from the N-terminal Cys2 to the C-terminal Tyr37. The high-resolution of the density map also allows us to distinguish two distinct rotamers of Arg11 and His18 residues.

The Phe23 residue within the FGAIL region is crucial for the structural integrity of the A25P-P1 fibrils, as the residues are located at the interface of all three filaments, thus facilitating stabilization of the core through hydrophobic interactions (Fig. 2b). This stabilization at the core is enhanced by the interaction between Tyr37 and Ile26. Following the proline-induced turn, Leu27 from the same strand engages in hydrophobic interactions with Leu12, Phe15, and Val17 from adjacent strands. Despite the proline being in the near vicinity and enforcing a loop towards the C-terminus, it does not prohibit the peptide from forming a short β-sheet. In fact, such formations are frequently observed in our data. Additional stabilizations to the structure are provided by ladder-like interactions formed by Gln10, His18, Asn21, and Asn22. These interactions are essentially H-bonds forming between corresponding amino acids in adjacent layers. In A25P-P1, β-sheets span three regions, i.e. Thr6-Leu12, Phe15-Asn22, and Ile26-Asn31, respectively. Interestingly, one of the cysteines, usually thought to be part of a completely disordered and flexible N-terminal region (PDB 6Y1A, 7M61, 7M64), is also a part of the β-sheet conformation.[22,25]

In terms of H-bonding interactions, Ser20 forms a bond with Tyr37 located two layers below, whereas Thr30 H-bonds to Asn35 are located in the upper layer. The terminal Tyr37 residue is wrapped inside and locked by H-bonding interactions to Asn35 on the adjacent layer (Fig. 2c, d). H-bonding interactions are also present between the side chain of Ser28 and the backbone oxygen of Ala8 on a separate chain, which may also lead to the increased stabilization of the structure.

Closer inspection of the A25P-P1 density map reveals a distinct region of unmodeled density within a pocket surrounding the His18 residues. This density cannot be fitted to alternative conformations of the polypeptide chain. Histidine residues are well-known coordination sites for metal ions and small molecules, and similar ligand-binding pockets have been observed in other amyloid structures, such as tau.[49] In our study, HEPES buffer molecule is the only molecule that may give rise to such elongated densities. It possesses charged sulfonate group and a free hydroxyl which can both donate and accept H-bonds to both His18 and the neighbouring Ser34. However, this interpretation requires further experimental validation.

hIAPP-S28P-P1 (PDB 8RM8). The structure of the first polymorph of S28P mutant constitute the majority of particles, indicating a predominant filament orientation for S28P. This specificity could partially explain the observed slow aggregation kinetics, as the peptides are confined to a specific arrangement. Interestingly, chain B of S28P-P1 displays a chain arrangement reminiscent of the double-S polymorph observed in WT hIAPP (TW3[25]), albeit with a slightly distorted symmetry. A defining feature of this assembly is the inward wrapping of the C-terminal Tyr37 into the amyloid core.

For S28P-P1 (Fig. 2c-d), the C-terminus is stabilized through H-bonding interactions between Thr30 and Tyr37 of chain A, anchoring Tyr37 in place. The position of Tyr37 is further supported by an additional H-bonding between Pro28

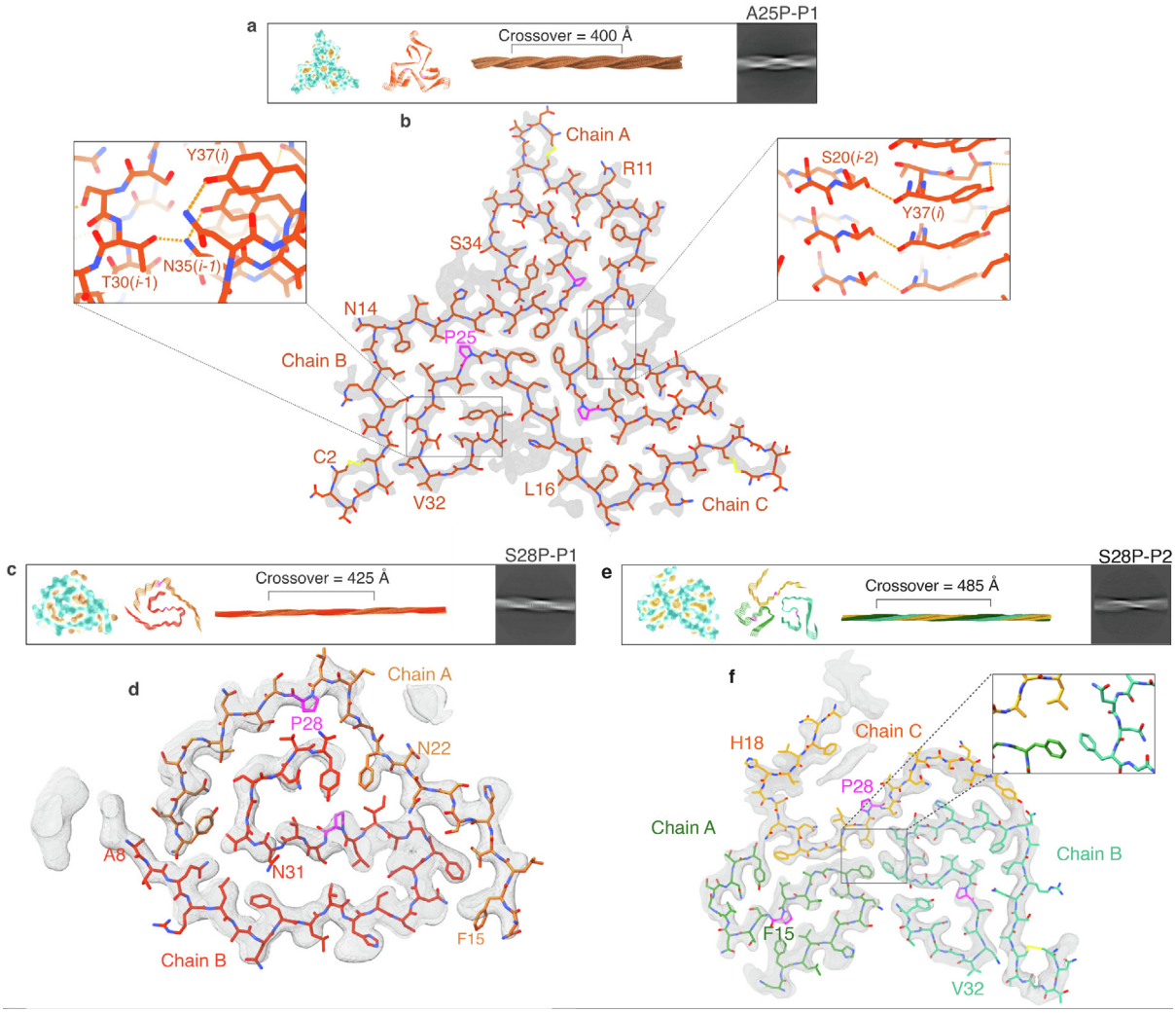

Fig. 2. Cryo-EM structures of hIAPP A25P and S28P mutants. Density and atomic model of a cross-section along the fibril axis for the A25P mutant and two mutants of S28P (a) Left shows the surface map for A25P-P1 with hydrophilic and hydrophobic regions in blue and yellow respectively. The adjacent fibril top view represents the main carbon chains with β-sheets indicated as arrows. To the right, fibril reconstruction for the corresponding structure and a representative 2D class average. b) A25P-P1 trimeric structure solved at 3.05 Å resolution with clear density from Cys2 to Tyr37. Disulfide bridges between C2 and C7 are highlighted in yellow. The core of the structure is held together by three Phe23 residues. Insets show Tyr37 is locked in place through H-bonding with Asn35 and interacting with Ser20 two layers above. (c) Same as (a) for S28P-P1. (d) Structure of S28P-P1 polymorph solved at 3.00 Å resolution. Tyr37 in chain B interacts with the backbone of the proline mutation highlighted in magenta. (e) Same as a) for S28P-P2. (f) Structure of S28P-P2 dimer solved at 3.60 Å resolution. The main hydrophobic interactions at the core are highlighted in the inset.

backbone oxygen and both Thr30 and Tyr37. In contrast, the Pro28 residue in chain B is spatially offset from Tyr37 and does not participate in the same interaction. Tyr37 of chain B exhibits a similar wrap towards the interface between chains A and B, but is instead forming a H-bond with Asn35. Furthermore, hydrophobic contacts, particularly between Phe23 in chain A and Tyr37 in chain B, enhance the integrity of the protofilament.

Fitted residues extend from Asn14 to Tyr37 for chain A and from Ala8 to Tyr37 for chain B. Asn31 from chain A is the sole contributor to ladder-like interlayer stabilization. Noteworthy, two distinct rotameric conformations are evident for His18 in chain A, reflecting local heterogeneity. β-sheets of chain A span from Gln10 to Ala13 and Phe15 to Ser20, while those of chain B form from His18 to Phe23 and Gly33 to Thr36.

hIAPP-S28P-P2 (PDB 8RM9). The second polymorph of the S28P mutant, S28P-P2, adopts a trimeric assembly composed of three distinct chains (Fig. 2e-f). In this structure, two chains (designated A and B) adopt distorted S-shaped conformations similar to those seen in the double-

S polymorph of WT hIAPP, whereas a third chain (chain C) wraps around the assembly of the other two chains. This wrap-around chain is stabilized by an extensive network of hydrophobic interactions involving key residues. Most important for the stability of the trimer are residues Phe23 (from chain A and B) and Leu27 (from chain C), which together form central hydrophobic cluster. Additionally, interactions between Phe15 of chain C and Tyr37 of chain A and between Phe15 and Leu27 both located on chain B further reinforce the assembly—mirroring the hydrophobic stabilization observed in the WT structure.

As in S28P-P1, the C-terminal Tyr37 in S28P-P2 is directed inward and participates in a H-bond with Thr30 in chain A. Despite the overall similarity between chains A and B, a distinct difference is observed in the orientation of Pro28. In chain A, Pro28 is directed away from Tyr37, which allows the formation of the Thr30-Tyr37 H-bond, whereas in chain B, Pro28 points towards Tyr37 and that changes the shape of the resulting loop towards the C-terminus. Additional weaker H-bonds are found between backbone carbonyls and Asn residues. The resolved density allowed fitting of residues from Asn14 to Tyr37 in chain A, from Thr9 to Tyr37 in chain B, and from Ala13 to Tyr37 in chain C. In this polymorph, the β-sheet structure is predominantly localized to the region spanning from Phe15 toward the FGAIL motif.

hIAPP-S29P-P1 (PDB 8QVP). For S29P mutant, we have resolved three high-resolution structures (Fig. 3). The first structure exhibits a C2 symmetry where the core features a steric zipper interaction between residues Phe15 to Phe23, further supported by an extensive network of H-bonds (Fig. 3b). His18 is involved in H-bonding with Ser20 and Asn31 from an adjacent layer, while Ser19 establishes a H-bond with Ser20 from a different protofilament (Fig. 3b). Additionally, Asn14 forms a H-bond with the backbone of Thr36. Phe15 from chain A engages in a hydrophobic interaction with Leu12 Phe15 and Val17 from chain B, stabilizing the interface between β sheets. The N-terminus is supported by the H-bonding between Gln10 and the backbone oxygen of Phe15 from another protofilament. Furthermore, Gln10 and Asn22 form a ladder-like structure respectively.

The residues are fitted from residue Ala8 to Tyr37, with the β sheets spanning from Gln10-Leu12, Asn14-Ser19, and Thr30-Ser34. The density also shows an alternative rotamer at His18 (Fig. 3b).

hIAPP-S29P-P2 (PDB 8QVQ). The S29P-P2 structure is another trimeric assembly; however it deviates from C3 symmetry by a narrow shift in

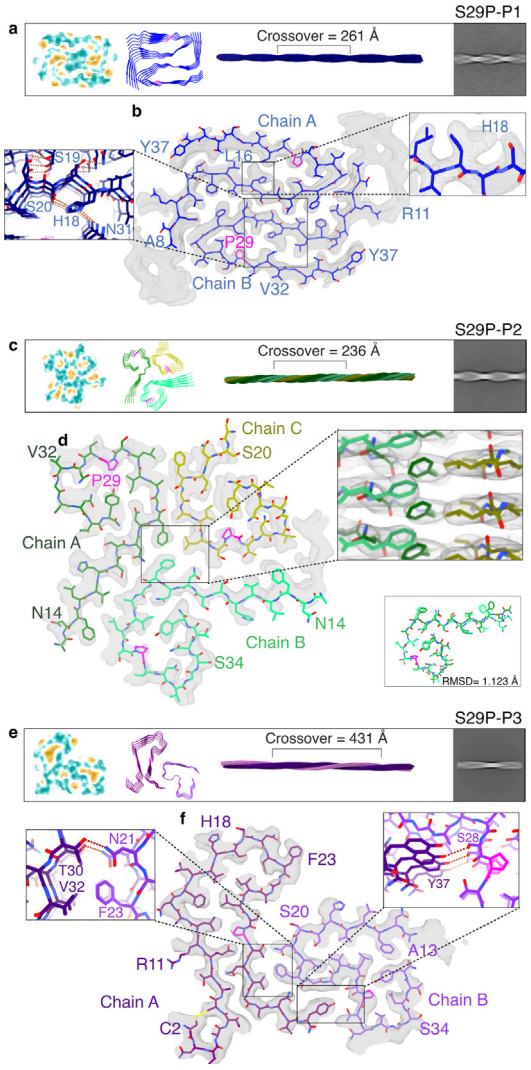

Fig. 3. Cryo-EM structures of hIAPP S29P mutant. Density and atomic model of a cross-section along the fibril axis for 3 structures of S29P. (a) Left shows the surface map for S29P-P1 with hydrophilic and hydrophobic regions in blue and yellow respectively. The adjacent fibril top view represents the main carbon chains with β-sheets indicated as arrows. To the right, fibril reconstruction for the corresponding structure and a representative 2D class average. (b) Structure of S29P-P1 C2 dimer solved at 3.75 Å resolution which is mostly stabilized by the large H-bonding network in the core. His18 can adopt two rotamers and forms H-bond with two residues from one layer below (Ser20 and Asn31) as shown in the insets. (c) Same as (a) for S29P-P2. (d) C1 trimeric structure of S29P-P2 solved at 3.44 Å resolution. The hydrophobic core of S29P-P2 is shown in the inset. The overlay of chains A and B yields a RMSD of approximately 1.1 Å. (e) Same as (a) for S29P-P3. f) Structure of S29P-P3 dimer solved at 3.25 Å resolution. The insets highlight the interactions between both chains.

the sequence of chain C (Fig. 3c-d). Chains A and B exhibit a similar arrangement with Phe23 at the center of their hydrophobic interactions. However, chain C introduces a variance with Leu27 contributing to the stability of the core (Fig. 3d). When aligned, chains A and B are almost identical in the backbone, with some residues only differing by local rotamers. The measured RMSD amounts to approx. 1.123Å.

For chains A and B, the amino acid sequence fitting is identical, extending from Asn14 to Tyr37. Chain C, on the other hand, presents a shorter fitted sequence, spanning from Ser19 to Tyr37. The hydrophobic cores within the chains are reinforced by interactions involving Ile26 and Tyr37.

An interesting aspect of this structure is the varied alignment of the protofilament layers: chains A and C align on one plane, while chain B is staggered, positioned between layers A and C (Fig. 3d). Both chains A and B feature a β-sheet region from Asn14 to Phe23, with chain B also including a segment from Ile26 to Leu27, a feature shared with chain C. The structural integrity here relies predominantly on hydrophobic interactions, with minimal H-bonding observed-only a single H-bond is noted between Ser19 of chain B and Ser28 of chain C. Additionally, a ladder-like formation involving Asn22 across each chain contributes to the overall stabilization of the trimeric assembly.

hIAPP-S29P-P3 (PDB 8QVR). The P3 polymorph of the S29P mutant resembles the TW4 model (PDB 7M65) identified in a prior study by Cao et al.[25] Chain A mirrors the TW4 protofilament with the entire amino acid sequence accurately matching the density (see Fig. S12 for detailed comparison). The distinctive feature is the domain inversion in chain B (Fig. 3e-f), which is fitted from Leu12 to Tyr37.

Within chain A, a disulfide bond between Cys2 and Cys7 provides N-terminal stability (Fig. 3f). The presence of hydrophobic residues such as Leu12, Phe15, Val17, Ile26, and Leu27 induces a turn, crafting a reverse 'U' shape within the protofilament. Thr6 of chain A further consolidates this architecture through H-bonding with Ser34. For chain B, the hydrophobic core is composed of Phe15, Val17, Ile26, Leu27, and Tyr37.

Interchain interactions include a modest hydrophobic connection between Val32 of chain A and Phe23 of chain B. The structural stability is enhanced by two key H-bonds: one between Thr30 of chain A and Asn21 of chain B, and another linking Tyr37 of chain A to Ser28 of chain B. The β-sheets within chain A extend from Ala8 to Ala13, Phe15 to Ser20, and Thr30 to Thr36, while in chain B, the sheets are defined from Asn14 to Ser20.

Design and characterization of non-amyloidogenic IAPP

Guided by the structural models of the proline mutants and the previously published WT hIAPP fibrils, we formulated a targeted strategy to disrupt key interactions within the amyloid assemblies. Our approach prioritized two fundamental structural determinants of fibril stability. In the first place, our primary focus was placed on residues comprising the interfaces stabilized by hydrophobic interactions. Secondly, we identified critical H-bonding interactions that stabilized the C-terminal regions of the peptide. The principal aim was to introduce sequence modifications that would destabilize these interactions and inhibit the formation of extended fibrillar structures. Our design strategy led to two distinct sets of mutations, one based on the structure of the trimeric A25P mutant, and one based on the two solved S28P models. Both designs were supported by simulations of amyloidogenic propensities using ZipperDB (shown in Fig. S15).[50]

In the case of the A25P-P1 structure, the central Phe23 residue, which forms a symmetric hydrophobic core, draws particular attention. Phe23 plays a crucial role in nearly every polymorph resolved in this study. To introduce both electrostatic and steric repulsion at the very center of the A25P-P1 structure, we replaced Phe23 with arginine. As a control, we also synthesized a single F23R mutant of IAPP to verify that the combination of both mutations is necessary to achieve a non-amyloidogenic effect, ensuring that amyloid inhibition is not solely due to that single mutation.

Having tested the extensive destabilization of the central hydrophobic region in the A25P-based double mutant, we next explored whether targeting additional residues outside the FGAIL core could also suppress fibrillization. To achieve this, we attempted to design a new model based on structural insights from S28P polymorphs. Similar to A25P-P1, Phe23 contributes to stabilizing the central hydrophobic interface, supporting a two-chain assembly in S28P-P1 and a three-chain assembly in S28P-P2. However, rather than applying the same mutation strategy, we identified that hydrophobic interactions outside the central core, particularly those involving Tyr37, might be equally important for fibril stability.

Here, we retained the FGAIL motif but mutated Phe15 to Ala, as our S28P models revealed that Phe15, Phe23, and Leu17 form a peripheral hydrophobic cluster. Substituting Phe15 with Ala reduces aromatic stacking and hydrophobic surface area without introducing a bulky or charged side chain that could potentially interfere with receptor binding, as the position is closer to

some of the key residues responsible for binding activity. Additionally, all S28P structures showed C-terminal Tyr37 residues forming H-bonds or engaging in hydrophobic interactions. Therefore, we mutate Tyr37 to Pro, yielding F15A S28P Y37P mutant of IAPP. It is important to note that Tyr37 has been mutated to proline in one of the latest drug analogs (Cagrilintide), a modification that improved binding of the drug to the Calcitonin G protein-coupled receptor (CTR).[17]

To evaluate the impact of these mutations on amyloid fibril formation, we monitored aggregation kinetics using ThT fluorescence under conditions identical to those employed for the WT peptide and Pramlintide (Fig. 4a). Notably, the F23R A25P double mutant did not exhibit any increase in ThT fluorescence, even after extended incubation periods of up to several weeks at the concentratioon of 200 μM, indicating a complete inhibition of fibril formation. Unlike the other constructs, the F23R A25P mutant shows no aggregation even in PBS buffer or under high-salt conditions (Fig. S3). In contrast, Pramlintide, a clinically used Amylin analog, formed fibrils within 40 h when measured at 100 μM, confirming its slower but nonetheless observable amyloidogenesis.

The triple mutant F15A S28P Y37P presented distinct aggregation kinetics, characterized by a relatively short initial lag phase (18.49 $\pm$ 0.03 h) followed by a strikingly long elongation phase that spanned 200 h (Fig. 4b). The t_{50} was estimated to be equal to 44.5 $\pm$ 0.5 h. At the end of the aggregation, the ThT fluorescence signal exceeded that of the WT hIAPP measurements, although this may be attributed to concentration difference. Atomic force microscopy (AFM) imaging (inset of Fig. 4b) revealed extensive regions populated by featureless aggregates, yet higher-resolution views demonstrated that these were composed of small, clustered fibrils typically around 100–200 nm in length. Thus, although the triple mutant ultimately forms fibrillar assemblies, the mutations appear to restrict fibril elongation and favor shorter aggregation products.

Due to the highly promising results obtained for the F23R A25P mutant, we next tested whether it was resistant to aggregation under conditions more relevant to physiological environments. Fig. 4c shows that even in RPMI cell culture medium, which contains elevated salt levels and glucose, the designed mutant remains non-aggregating over the studied timeframe. Furthermore, the addition of pre-formed WT hIAPP fibril seeds failed to initiate fibril growth in this double mutant, indicating the true non-amyloidogenic behaviour of the designed sequence.

All aggregation products were additionally visualized by AFM (Fig. 4d). Consistent with the ThT assays, WT hIAPP, Pramlintide, and the F23R single mutant showed fibrillar networks, though F23R alone formed visibly shorter fibrils. On the other hand, we detected no fibrils for the double mutant.

From a therapeutic perspective, it is critical to assess whether the designed IAPP mutants not only prevent amyloid fibril formation but also remain non-toxic to pancreatic β- cells. To test for cytotoxicity, we performed MTT assays using MIN6 pancreatic β-cells (Fig. 4e). The cell line was treated with non-amyloidogenic rat IAPP, Pramlintide, WT hIAPP, F23R A25P IAPP, and F15A S28P Y37P IAPP. The results demonstrated that while hIAPP significantly reduced cell viability by 50 %, this effect was effectively abolished in the designed peptides. These findings are consistent with the reduced aggregation kinetics of the mutant forms and underscore their therapeutic potential.

Discussion

Sequence-structure relationship in IAPP amyloidogenesis

The results presented in our study provide a comprehensive comparison between the amyloid fibril structures of WT IAPP and its proline mutants. Our study reveals that even subtle sequence modifications can dramatically affect interactions and lead to the formation of unique fibril polymorphs.

Traditionally, the FGAIL region has been considered the true amyloid core of hIAPP. It has been found to form amyloids by itself,[51] participate in the formation of oligomeric intermediates,[52,53] and takes an important stabilizing role in IAPP fibrils as evidenced by the solved cryo-EM structures of the WT IAPP[25,27] and our current work. In most WT structures, the amyloid β-sheet is located in the FGAIL region; if not, the FGAIL region constitutes a hydrophobic core at the filament interface. At the same time, the residues preceding the FGAIL region, specifically His18-Asn22, are not involved in the formation of β-sheets.

However, as we show in Fig. 5, nearly all proline-substituted structures develop well-defined β-sheets extending from Phe15 to Asn22, a region that in the WT peptide lacks a stable secondary structure. This is an important observation because proline is typically known to disrupt β-sheets; yet, our data show that these mutations do not eliminate β-sheet formation and may even encourage their development just beyond the mutation site, either toward the C-terminus or at the boundary of the FGAIL region. These findings indicate that proline substitutions reshape the local structural framework, shifting the amyloid-forming region beyond the FGAIL and revealing a more complex relationship between sequence modifications and fibril assembly.

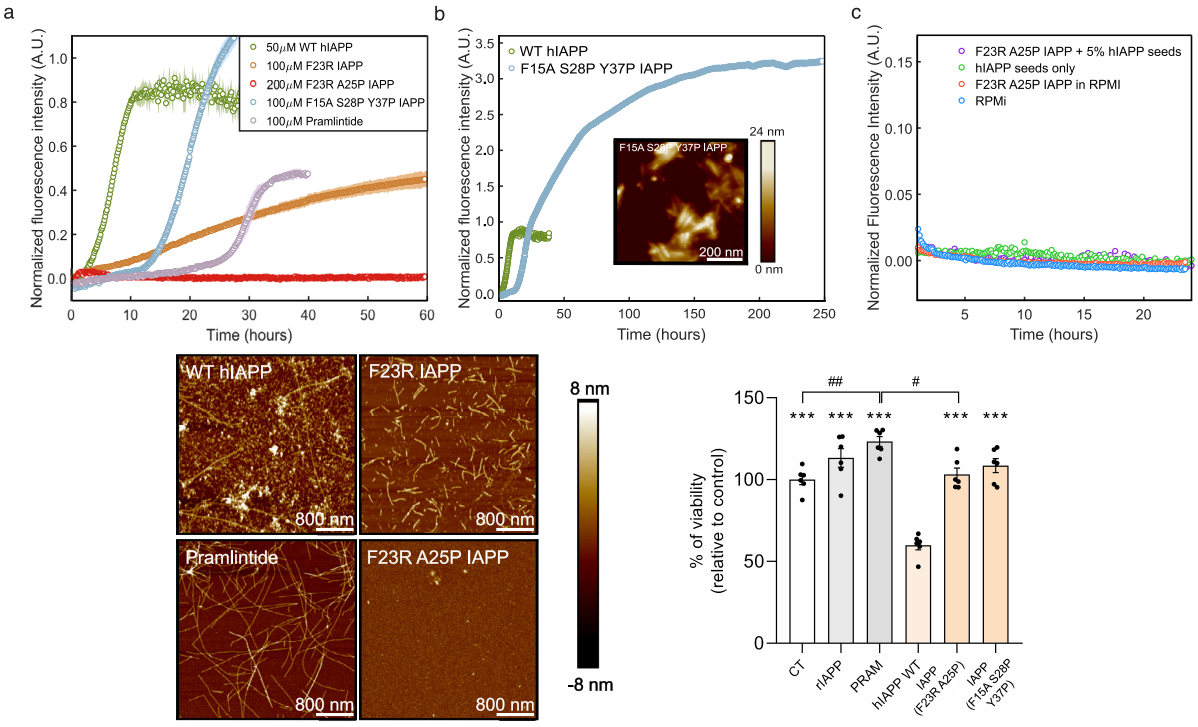

Fig. 4. Aggregation kinetics and cytotoxicity of the newly designed peptides F23R, F23R A25P and F15A S28P Y37P. (a) ThT-monitored aggregation kinetics showing a longer lag phase and a lower final intensity for all designed peptides except for the triple mutant. (b) Extended aggregation kinetics from (a) for the triple mutant compared with WT hIAPP showing a very long elongation phase. The resulting AFM image of the fibrils is given as inset (c) ThT-monitored kinetics of the double mutant revealed no aggregation under high salt conditions of the RPMI buffer and when seeded by WT hIAPP. (d) AFM images showing the fibrils formed by the WT and F23R IAPP and the absence of fibrillar structures in the F23R A25P double mutant, confirming the inhibitory effect of the additional mutation on the fibril formation. (e) Cell viability measured by MTT assay on the MIN6 cell line showing percentage of living cells after 36 h of treatment with rat IAPP (rIAPP), Pramlintide (PRAM), hIAPP, F23R A25P IAPP, and F15A S28P Y37P IAPP. All peptides were used at a final concentration of 20 μM. Bars represent values relative to untreated MIN6 cells (CT, given the value of 100 %) for $n = 2$ independent experiments performed in triplicate. # $p < 0.05$, ## $p < 0.01$, ***$p < 0.001$ respect to hIAPP, using one-way ANOVA followed by Tukey's post hoc test.

Apart from rodents and some primates, virtually all animal species carry Pro residue at position 29. This indicates that fibrillar polymorphs with extended β-sheets forming before the FGAIL region might predominate in islet amyloidosis across various species. Furthermore, the S20G mutation observed in the human population leads to fibrils that exhibit β-sheets in the His18-Asn22 region.[24] While this is not immediately apparent from the WT structures alone, it suggests that this region might indeed represent the significant part of the amyloidogenic core of IAPP. It appears that the prevailing assumption of the FGAIL region as the exclusive core of amyloidogenic activity may overlook the contributions of additional regions to fibril stability.

In order to map the structural landscape of the solved proline mutants in relation to previously characterized IAPP polymorphs from the Amyloid Atlas,[54] we performed a distance-based Principal Component Analysis (dPCA) on the common C_α core spanning residues 15 to 37. Detailed description on the implementation is provided in the Methods section. The resulting conformational map (Fig. 5b), where the first two principal components capture nearly 76 % of the total variance, reveals a wide and diverse distribution of structures, confirming the remarkable polymorphic nature of IAPP amyloid fibrils. Our newly solved proline mutants (marked by stars) are broadly scattered across the conformational space, indicating that each substitution drives the formation of a unique fibril architecture rather than converging on a common structural motif.

The analysis also highlights specific structural relationships and clusters. For instance, the S20G mutants form two distinct clusters at opposite ends of the PC1 axis. The S28P-P2 polymorph is structurally closest to the WT SS/TW3 polymorph, which is consistent with S28P-P2 forming a similar, albeit distorted, double S-shaped assembly. Furthermore, our S29P-P3 structure

clusters with one of the S20G polymorphs and the *ex vivo* elongated WT TW1 structure, suggesting the proline mutation has a similar effect on the fibril fold to that of S20G mutation, which is located on the opposite end of the FGAIL region.

To translate these principal components into specific structural features, we analyzed the component loadings (Fig. 5c). In this analysis, a positive loading (red) signifies that a high PC score is associated with a larger distance between a residue pair. On the other hand, a negative loading (blue) indicates that a high PC score corresponds to a smaller distance, or tighter packing. This interpretation allows us to deconstruct the structural differences. For example, polymorphs with a large positive PC1 score, such as S28P-P1, exhibit greater separation between residues in the central region (Phe15-Asn22) and the C-terminus. This observation is consistent with our cryo-EM model, in which the chain A wraps around the structure formed by chain B, essentially maximizing the distance between the opposite ends of the peptide sequence. A combination of positive PC1 and negative PC2 indicates a tight packing between the FGAIL region and the central part of the sequence, such as in chain A of S29P-P3, where the fragments are in direct interactions with each other following a loop. Therefore, this dPCA analysis not only classifies the global folds but also characterizes the specific residue-level interactions that define each unique structural signature.

Reflecting on this, our results suggest a broader scope of important regions influencing amyloid fibril formation, extending our knowledge base and offering fresh insights into the protein aggregation phenomena. This detailed structural information can be used to identify potential inhibition sites and to design non-amyloidogenic forms of IAPP that support existing therapies in type 2 diabetes.

Design considerations for preserving receptor binding

Beyond expanding our understanding of amyloid structure, these findings have direct implications for designing peptide-based therapeutics. Effective hIAPP analogs must balance two competing demands: maintaining receptor-binding function while preventing aggregation. The function of hIAPP is modulated through its binding

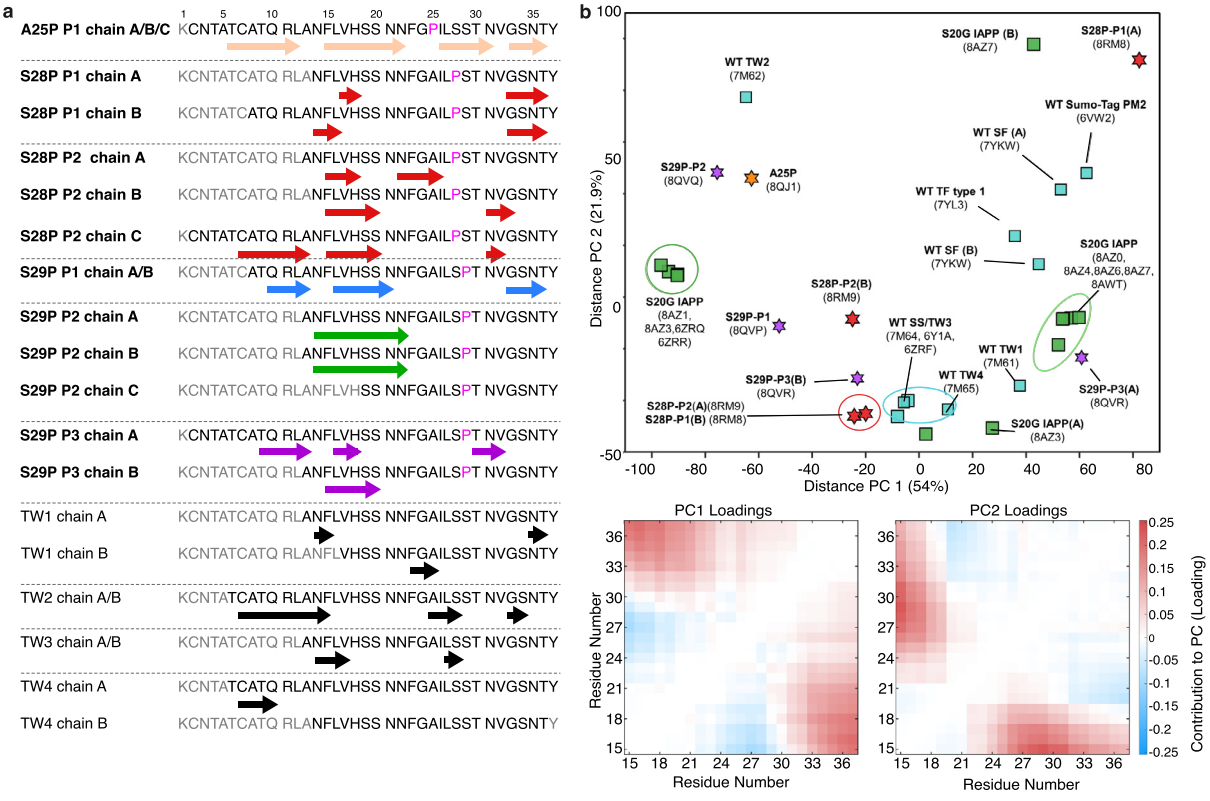

Fig. 5. (a) The analysis of the β-sheet regions in solved and published WT structures. β-sheets are denoted by colored arrows for mutated sequences and black arrows for WT structures from Cao et al. Residues not resolved with cryo-EM data are shown in gray. The proline mutations disrupt β-sheet formation in the FGAIL region but new β-sheets form in proximity to the mutations, particularly in the Phe15-Asn22 region. (b) Distance-based Principal Component Analysis (PCA) on the 23-residue common core of previously published IAPP structures (squares) and the mutants solved in this study (stars). PCA shows that the first two components capture 76 % of the total variance (dPC1 = 54.0 %; dPC2 = 21.9 %).

to calcitonin receptors (CTRs), which are members of the G-protein coupled receptors (GPCRs) family.[55,56] The binding mechanism is believed to adhere to the 'two-domain model of binding',[57] involving both the N- and C-termini in receptor activation. Designing active, non-amyloidogenic IAPP forms would require a complete prevention of amyloid formation while preserving the critical receptor-binding residues, particularly the N-terminal residues Thr6, Thr9, Arg11, and Leu12, and ensuring the high solubility and chemical stability of the peptide.

Our structural models provide numerous insights that may aid the design of non-amyloidogenic IAPP analogs with therapeutic potential. By selectively disrupting key hydrophobic contacts and H-bonding networks, such as replacing Phe23 with a charged residue, we demonstrate how targeted mutations influence aggregation behavior. However, the impact of introducing a charged residue near the FGAIL region on receptor interactions remains to be determined. While the F23R A25P analog exhibits strong non-amyloidogenic properties, a more conservative approach, such as substituting hydrophobic residues with alanine, may offer a less perturbative alternative. This strategy was applied in our design of the S28P-based triple mutant at a different position and could provide a viable means of maintaining receptor compatibility while reducing aggregation propensity.

Despite these structural modifications, the designed triple mutant retained the ability to form fibrils. This observation suggests that modifying the FGAIL region itself may be necessary for complete amyloid inhibition. Future advancements in cryo-EM methodologies and image analysis, or integration with complementary biophysical methods such as solid-state NMR, may allow comprehensive characterization of these additional fibril species, further enhancing our understanding of IAPP polymorphism and allowing for more refined design strategies.

Overall, the study highlights the effectiveness of cryo-EM in distinguishing multiple fibril polymorphs within the same sample, revealing the diverse structural landscapes that govern IAPP aggregation and the consequences of even minor sequence alterations.By systematically integrating detailed structural analyses, computational modeling, and experimental validation, our study advances structural research on amyloids and the rational design of IAPP therapeutics. This approach is particularly relevant not only in the context of type 2 diabetes but also in a broader range of diseases where the direct application of biologically active peptide species is limited by aggregation phenomena.

Materials and methods

Synthetic hIAPP mutants preparation

The peptides were synthesized on a 0.10 mmol scale using Fmoc solid phase peptide synthesis with a Intavis Multipep CF peptide synthesizer. Tentagel R RAM resin (0.21 mmol/equiv) was used to produce a C-terminal amide. Fmoc-Ala Thr(Psi(Me,Me) pro)-OH was used at positions 8, 9 and Fmoc-Leu-Ser(Psi(Me,Me) pro)-OH at positions 27, 28.[58] The synthesized peptide was cleaved with TFA:TIS:H2O (9.5 %, 2.5 %, 2.5 %), dissolved in H2O and lyophilized overnight. The crude peptides were dissolved in DMSO mixed with 25 % acetic acid solution at the 60:40 ratio for 24 h to form the disulfide bridge between C2 and C7. The oxidized peptides were purified using reverse-phase HPLC (Isera C18 preparative column, 250 x 20 mm), with a gradient elution composed of buffer A in 100 % H2O with 0.045 % HCl and buffer B in 80 % acetonitrile with 0.045 % HCl. The eluted peptides were collected and lyophilized overnight. Second purification was carried out by dissolving the peptides in 50 % hexafluoroisopropanol (HFIP) and 20 % acetic acid. The purified peptides were lyophilized overnight again. Mass spectrometry was used to confirm the mass of the purified peptides (Fig. S4). The peptides were dissolved in 100 % HFIP for several hours to monomerize the peptides, they were then aliquoted based on the concentration needed and lyophilized overnight and stored at −20°C until use. A combination of BCA (Bicinchoninic Acid) assay and native tyrosine absorption at 280 nm were used to determine the concentration of the aliquots.

Peptide aggregation kinetics using Thioflavin T

The concentration of ThT was determined by using absorbance at 416 nm with extinction coefficient of 32000 $M^{-1}cm^{-1}$ in H_2O. The kinetics assays were carried out in a Perkin Elmer Victor X4 with excitation wavelength set at 450 nm and emission wavelength set at 486 nm. The assays were conducted at 25 °C without shaking. The peptides were resuspended in 10 mM HEPES (pH 7.4). The final concentrations of the peptides were 25, 50, 100 μM, the concentration of ThT was 20 μM, and the total volume of each well was 100 μL. The assays were performed in a 96-well clear bottom plate and each peptide was run in triplicate. The fluorescence was measured every 5 min with bottom reading. Fluorescence assays on the designed mutants were additionally carried out in phosphate-buffered saline (PBS, *Fischer Sci.*) and in RPMI 1640 Medium without phenol red (*Gibco*^{TM})

Negative stained transmission electron microscope

The peptides were resuspended in 10 mM HEPES (pH 7.4) at either 50 or 100 μm concentration and incubated at room temperature without shaking for 7 days before staining. 5 μL of fibril was added to a freshly glow-discharged Formvar-coated carbon grid for five minutes, the excess sample was blotted, and the grids were stained with 0.75 % uranyl formate for 15 s. The grids were left to air dry. The imaging was performed with Talos L120V (Thermo Fisher) at the Centre for Cellular Imaging of Sahlgrenska Academy, University of Gothenburg (Fig. S5).

Atomic force microscopy (AFM)

Samples for AFM were prepared under the same conditions as those used in the ThT fluorescence assays and allowed to aggregate for at least 5 days. A 20 μL aliquot of each sample was deposited onto a mica substrate and incubated for 15 min. The substrate was then rinsed three times with 50 μL of deionized water and excess water was removed using a wiper (Kimwipe) after each wash. Images were acquired using a Bruker Dimension Icon (ICON4-SYS) atomic force microscope and processed using NanoScope Analysis software version 1.9.

Cryo-electron microscopy data collection and processing

The peptides were resuspended in 10 mM HEPES (pH 7.4) at 100 μM concentration and incubated at room temperature without shaking for 7 days. They were then applied to freshly glow-discharged carbon grids (Quantifoil Cu R2/2, 300 mesh), blotted with filter paper for 5 s and plunged frozen directly into liquid ethane with Vitrobot Mark IV (Thermo Fisher). The A25P was imaged with a 300 kV Titan Krios and collected on a Gatan K3 BioQuantum detector with a pixel size 0.828 Å, defocus values from −0.5 to −2 μm, and total electron dose of 39.849 e-/Å^2. The S28P was imaged with a 300 kV Titan Krios and collected on a Falcon 4i detector with a pixel size 0.704 Å, with defocus values from −1.2 to −2.4 μm, and total electron doses of 44.6 e-/Å^2. The S29P was imaged with a 300 kV Titan Krios and collected on a Gatan K2 BioQuantum detector with a pixel size 0.821 Å, defocus values from −0.6 to −2.4 μm, and total electron dose of 58 e-/Å^2. The movies were imported, motion corrected with RELION[45]'s implementation UCSF MotionCor2,[59] and estimated the contrast transfer function (CTF) using CTFFIND[60] in RELION 4.0.

For S29P, the fibrils were picked manually, extracted at a 768-pixel box down-sampled to a 256-pixel box, and underwent several rounds of 2D classification to separate the flat and twisted fibrils. For P1 and P2, the selected classes were re-extracted at a 352-pixel box and underwent multiple rounds of 2D classification. P1 and P2 were selected separately and underwent 3D classifications to further clean up the particles. An initial model of P1 and P2 was generated separately from relion_helix_inimodel script using classes from 2D classification. A 3D refinement with P1 was performed with a C2 symmetry and the map was postprocessed after. The 3D refinement of P2 was performed with a C1 symmetry. The particles were polished and the map was postprocessed.

For S29P P3, the fibrils were extracted from a 960-pixel box down-sampled to a 260-pixel box. Multiple rounds of 2D classification were used to separate the P3 from others. The selected particles were re-extracted at a 600-pixel box and down-sampled to a 300-pixel box. After multiple rounds of 3D classifications, the cleaned-up particles were re-extracted at a 352-pixel box and a 3D refinement with an initial model from 3D classifications was performed. The particles were polished, and the map was postprocessed.

For A25P, some fibrils were picked manually and extracted at a 400-pixel box, and a 2D classification was used to separate the flat and twisted fibrils. The twisted fibrils were used as a model for Topaz[44] training. After the training, all the fibrils were auto-picked with Topaz implemented for amyloid. The particles were extracted at a 960-pixel box down sampled in a 120-pixel box and underwent multiple rounds of 2D classification. Twisted fibrils were re-extracted at a 640-pixel box and down-sampled to a 320-pixel box. 2D classes were then used to further classify the polymorphs. The P1 polymorph was selected and re-extracted at a 352-pixel box. An initial model was generated from the relion_helix_inimodel script using classes from 2D classification. Several rounds of 3D classifications were used to further clean up the particles and the 3D refinement was performed with a C3 symmetry. The particles were polished, and the map was re-calibrated to 0.828 Å during postprocess step.

For S28P, the Topaz auto-picking model trained from A25P was used directly to auto-pick the fibrils. Once picked, the fibrils were extracted at a 960-pixel box down-sampled to a 240-pixel box, and underwent several rounds of 2D classifications. The twisted fibrils were re-extracted to a 720-pixel box down-sampled to a 360-pixel box and further cleaned up with several rounds of 2D classifications. The P1 polymorph was selected and re-extracted at a 320-pixel box. An initial model was generated from relion_helix_inimodel script using classes from 2D classification. The particles underwent multiple 3D classifications, and the 3D refinement was

performed with a C1 symmetry. The particles were polished, and the map was postprocessed. The resolution of the reconstructed maps was calculated based on the 0.143 Fourier shell correlation (FSC) criterion (Fig. S8). The five-layer reconstruction maps and schematic representative of all structures are shown in Fig. S9 and S10.

Model building and refinement

Prior to model building, density maps were sharpened with EMready2.[61] To ensure no artifacts are introduced to the maps, a direct comparison between unsharpened and sharpened maps are made and presented in Fig. S11. The atomic model of each structure was built de novo with COOT 0.9.8.[62] The backbone was built with baton building followed by C-alpha to the mainchain. The Ala amino acids were then mutated to respective amino acids. An OXT was added on the C-terminal Tyr of each structure and later modified to NH2 to include the C-terminal amide group. The single-layer model was refined alternating both real space refine zone in COOT and real-space refinement in PHENIX.[63] Once the single-layer model was optimized with low Ramachandran outliers and clashes, an additional four layers were duplicated in COOT to a five-layer model. The final model was refined using real-space refinement in PHENIX with non-crystallographic symmetry (NCS) constraint for secondary structure and repeating layers. The H-bonding within the models was calculated with HBPLUS v.3.06. The final refinement parameters are shown in Table 1.

MIN6 cell line culture and cell viability assay

The mouse pancreatic beta cell line MIN6 was maintained in Dulbecco's modified Eagle medium (Sigma–Aldrich) containing 25 mM glucose and supplemented with 10 % fetal bovine serum (v/v), 2 mM L-glutamine, 100 U/mL penicillin, 100 mg/mL streptomycin, and 50 μM β-mercaptoethanol at 37 °C under 5 % CO_2 atmosphere. For assessing cell viability, MIN6 cells were plated onto 96-well plates (50 k cells per well) for MTT assay. Cells were cultured in the presence of the different IAPP forms at the indicated concentrations for 36 h. Then, plates were incubated with medium containing 0.75 mg/ml of 3-(4,5-dimethythiazol-2-yl)-2,5-diphenyltetrazolium bromide (MTT) for 2 h at 37 °C. The resulting formazan crystals were solubilized in Isopropanol/0.04 N HCl solution and optical density was read at 575 and 650 nm using an Infinite®M Plex, multimode microplate reader (TECAN, Switzerland). The survival rate was calculated as the OD 575–650 difference and expressed relative to untreated MIN6 cells, which were given the value of 100 %.

Distance-based principal-component analysis (dPCA) of IAPP fibril models

The analysis included a set of experimental cryo-EM structures, comprising our newly solved mutants and previously published models from the Amyloid Atlas. A common C_α core of 23 residues was first identified across all structures. To ensure that each unique structural fold was represented appropriately, a protocol was implemented to automatically identify and select representative protofilaments from each fibril entry. For a given PDB entry, all constituent chains containing the common core were extracted, and their structural similarity was quantified via an all-vs-all C_α root-mean-square deviation (RMSD) matrix. These chains were then grouped into structural clusters using the DBSCAN algorithm with an RMSD threshold of 1.0Å. From each of these structural clusters, a single representative protofilament was selected for the final analysis. This representative was determined by identifying the medoid of the cluster, which is the chain with the minimum average RMSD to all other chains within that same cluster. This process ensures that symmetric assemblies, where all chains fall into a single cluster, contribute one representative to the analysis, while asymmetric assemblies, whose chains form multiple distinct clusters, contribute one representative per unique fold. For each of these final representative protofilaments, a vector of all internal C_α-C_α distances was calculated from its unaligned coordinates. These distance vectors were compiled into a matrix, and Principal Component Analysis was performed. The principal components (loadings) from this analysis, which describe the contribution of each residue-residue distance pair to the overall structural variance, were reshaped into square matrices for visualization. All steps were executed using custom Python scripts.

Data availability statement

Structural data have been deposited into the Worldwide Protein Data Bank (wwPDB) and the Electron Microscopy Data Bank (EMDB) with the following accession codes: PDB QJ1, 8RM8, 8RM9, 8QVP, 8QVQ and 8QVR; and EMDB-18441, 19353, 19354, 18671, 18672 and 18673.

CRediT authorship contribution statement

Anna Novials: Methodology, Investigation.**Joan Marc Servitja**: Methodology, Investigation. **Sebastian Westenhoff**: Validation, Funding acquisition. **Alesia A Tietze**: Methodology. **Dylan Valli**: Methodology, Investigation, Formal analysis,

Data curation. **Mikolaj Ignacy Kuska**: Data curation, Investigation, Visualization, Writing - review & editing. **Michal Maj**: Writing – review & editing, Writing – original draft, Visualization, Validation, Supervision, Software, Resources, Project administration, Methodology, Investigation, Funding acquisition, Formal analysis, Data curation, Conceptualization.**Saik Ann Ooi**: Writing – review & editing, Visualization, Validation, Methodology, Investigation, Formal analysis, Data curation.**Helena Marí**: Methodology, Investigation, Formal analysis, Data curation.**Himanshu Chaudhary**: Validation, Supervision, Investigation. **Weixiao Yuan Wahlgren**: Visualization, Validation, Supervision.

DECLARATION OF COMPETING INTEREST

The authors declare that they have no known competing financial interests or personal relationships that could have appeared to influence the work reported in this paper.

Acknowledgements

MM acknowledges the Swedish Research Council (Grant No. VR 2020–05403), the Swedish Society for Medical Research (S20-0156), and Harald and Greta Jeanssons Foundation Grant (J2021-0114). We acknowledge the Centre for Cellular Imaging at the University of Gothenburg and the National Microscopy Infrastructure, NMI (VR-RFI 2019–00217) for assisting in microscopy. We acknowledge the use of the Cryo-EM Uppsala facility for grid preparation and cryo-EM screening, funded by the Department of Cell and Molecular Biology, the Disciplinary Domains of Science and Technology and of Medicine and Pharmacy at Uppsala University. The data was collected at the Cryo-EM Swedish National Facility funded by the Knut and Alice Wallenberg, Family Erling Persson and Kempe Foundations, SciLifeLab, Stockholm University and Umeå University. The computations were enabled by resources provided by the National Academic Infrastructure for Supercomputing in Sweden (NAISS) at Uppsala University and Linköping University partially funded by the Swedish Research Council through grant agreement No. 2022–06725 (NAISS) and 2018–06479 (PReSTO). Computing time was provided to M. M. with the following grants: NAISS 2023/5–165, NAISS 2023/6–112, NAISS 2024/6–150, NAISS 2023/22–1272, Berzelius-2023–271 and Berzelius-2023–77. This study was funded by Instituto de Salud Carlos III (ISCIII) to A.N. and J.-M.S. (project PI20-00658, co-funded by the European Union), and by the European Federation for the Study of Diabetes (EFSD)/ Boehringer Ingelheim European Research Programme to J.-M.S.

Appendix A. Supplementary data

Supplementary data associated with this article can be found, in the online version, athttps://doi.org/10.1016/j.jmb.2025.169405.

Received 24 April 2025;
Accepted 19 August 2025;
Available online 22 August 2025

Keywords:
amyloid;
hIAPP;
cryo-EM;
type 2 diabetes

References

1. Iadanza, M.G., Jackson, M.P., Hewitt, E.W., Ranson, N.A., Radford, S.E., (2018). A new era for understanding amyloid structures and disease. *Nat. Rev. Mol. Cell Biol.* **19** (12), 755–773.
2. Jaikaran, E.T., Clark, A., (2001). Islet amyloid and type 2 diabetes: from molecular misfolding to islet pathophysiology. *Biochim. Biophys. Acta, Mol. Basis Dis.* **1537** (3), 179–203.
3. Westermark, P., Wilander, E., (1983). Islet amyloid in type 2 (non-insulin-dependent) diabetes is related to insulin. *Diabetologia* **24** (5), 342–346.
4. Höppener, J.W., Ahrén, B., Lips, C.J., (2000). Islet amyloid and type 2 diabetes mellitus. *N. Engl. J. Med.* **343** (6), 411–419.
5. Hayden, M.R., Tyagi, S.C., (2001). A is for amylin and amyloid in type 2 diabetes mellitus. *JOP* **2** (4), 124–139.
6. Clark, A., Nilsson, M., (2004). Islet amyloid: a complication of islet dysfunction or an aetiological factor in Type 2 diabetes?. *Diabetologia* **47**, 157–169.
7. Alrouji, M., Al-Kuraishy, H.M., Al-Gareeb, A.I., Alexiou, A., Papadakis, M., Saad, H.M., Batiha, G.E.-S., (2023). The potential role of human islet amyloid polypeptide in type 2 diabetes mellitus and Alzheimer's diseases. *Diabetol. Metabolic Syndrome* **15** (1), 101.
8. Irvine, G.B., El-Agnaf, O.M., Shankar, G.M., Walsh, D.M., (2008). Protein aggregation in the brain: the molecular basis for Alzheimer's and Parkinson's diseases. *Mol. Med.* **14**, 451–464.
9. Schmitz, O., Brock, B., Rungby, J., (2004). Amylin agonists: a novel approach in the treatment of diabetes. *Diabetes* **53** (suppl_3), S233–S238.
10. Westermark, P., Eizirik, D.L., Pipeleers, D.G., Hellerström, C., Andersson, A., (1995). Rapid deposition of amyloid in human islets transplanted into nude mice. *Diabetologia* **38** (5), 543–549.
11. Tatarek-Nossol, M., Yan, L.-M., Schmauder, A., Tenidis, K., Westermark, G., Kapurniotu, A., (2005). Inhibition of hIAPP amyloid-fibril formation and apoptotic cell death by a designed hIAPP amyloid-core-containing hexapeptide. *Chem. Biol.* **12** (7), 797–809.

12. Wang, H., Abedini, A., Ruzsicska, B., Raleigh, D.P., (2014). Rationally designed, nontoxic, nonamyloidogenic analogues of human islet amyloid polypeptide with improved solubility. *Biochemistry* **53** (37), 5876–5884.
13. Betsholtz, C., Svensson, V., Rorsman, F., Engström, U., Westermark, G.T., Wilander, E., Johnson, K., Westermark, P., (1989). Islet amyloid polypeptide (IAPP): cDNA cloning and identification of an amyloidogenic region associated with the species-specific occurrence of age-related diabetes mellitus. *Exp. Cell. Res.* **183** (2), 484–493.
14. Cao, P., Abedini, A., Raleigh, D.P., (2013). Aggregation of islet amyloid polypeptide: from physical chemistry to cell biology. *Curr. Opin. Struct. Biol.* **23** (1), 82–89.
15. Pullman, J., Darsow, T., Frias, J.P., (2006). Pramlintide in the management of insulin-using patients with type 2 and type 1 diabetes. *Vasc. Health Risk Manag.* **2** (3), 203–212.
16. Bower, R.L., Hay, D.L., (2016). Amylin structure–function relationships and receptor pharmacology: implications for amylin mimetic drug development. *Br. J. Pharmacol.* **173** (12), 1883–1898.
17. Kruse, T., Hansen, J.L., Dahl, K., Schaffer, L., Sensfuss, U., Poulsen, C., Schlein, M., Hansen, A.M.K., Jeppesen, C. B., Dornonville de la Cour, C., et al., (2021). Development of cagrilintide, a long-acting amylin analogue. *J. Med. Chem.* **64** (15), 11183–11194.
18. He, S., Scheres, S.H., (2017). Helical reconstruction in RELION. *J. Struct. Biol.* **198** (3), 163–176.
19. Lövestam, S., Scheres, S.H., (2022). High-throughput cryo-EM structure determination of amyloids. *Faraday Discuss.* **240**, 243–260.
20. Fitzpatrick, A.W., Falcon, B., He, S., Murzin, A.G., Murshudov, G., Garringer, H.J., Crowther, R.A., Ghetti, B., Goedert, M., Scheres, S.H., (2017). Cryo-EM structures of tau filaments from Alzheimer's disease. *Nature* **547** (7662), 185–190.
21. Lövestam, S., Koh, F.A., van Knippenberg, B., Kotecha, A., Murzin, A.G., Goedert, M., Scheres, S.H., (2022). Assembly of recombinant tau into filaments identical to those of Alzheimer's disease and chronic traumatic encephalopathy. *Elife* **11**, e76494.
22. Röder, C., Kupreichyk, T., Gremer, L., Schäfer, L.U., Pothula, K.R., Ravelli, R.B., Willbold, D., Hoyer, W., Schröder, G.F., (2020). Cryo-EM structure of islet amyloid polypeptide fibrils reveals similarities with amyloid-β fibrils. *Nat. Struct. Mol. Biol.* **27** (7), 660–667.
23. Cao, Q., Boyer, D.R., Sawaya, M.R., Ge, P., Eisenberg, D. S., (2020). Cryo-EM structure and inhibitor design of human IAPP (amylin) fibrils. *Nat. Struct. Mol. Biol.* **27** (7), 653–659.
24. Gallardo, R., Iadanza, M.G., Xu, Y., Heath, G.R., Foster, R., Radford, S.E., Ranson, N.A., (2020). Fibril structures of diabetes-related amylin variants reveal a basis for surface-templated assembly. *Nat. Struct. Mol. Biol.* **27** (11), 1048–1056.
25. Cao, Q., Boyer, D.R., Sawaya, M.R., Abskharon, R., Saelices, L., Nguyen, B.A., Lu, J., Murray, K.A., Kandeel, F., Eisenberg, D.S., (2021). Cryo-EM structures of hIAPP fibrils seeded by patient-extracted fibrils reveal new polymorphs and conserved fibril cores. *Nat. Struct. Mol. Biol.* **28** (9), 724–730.
26. Li, D., Zhang, X., Wang, Y., Zhang, H., Song, K., Bao, K., Zhu, P., (2022). A new polymorphism of human amylin fibrils with similar protofilaments and a conserved core. *Iscience* **25** (12)
27. Wilkinson, M., Xu, Y., Thacker, D., Taylor, A.I., Fisher, D. G., Gallardo, R.U., Radford, S.E., Ranson, N.A., (2023). Structural evolution of fibril polymorphs during amyloid assembly. *Cell* **186** (26), 5798–5811.
28. Li, S.-C., Goto, N.K., Williams, K.A., Deber, C.M., (1996). Alpha-helical, but not beta-sheet, propensity of proline is determined by peptide environment. *Proc. Natl. Acad. Sci. U.S.A.* **93** (13), 6676–6681.
29. Wang, H., Ridgway, Z., Cao, P., Ruzsicska, B., Raleigh, D. P., (2015). Analysis of the ability of pramlintide to inhibit amyloid formation by human islet amyloid polypeptide reveals a balance between optimal recognition and reduced amyloidogenicity. *Biochemistry* **54** (44), 6704–6711.
30. Ridgway, Z., Eldrid, C., Zhyvoloup, A., Ben-Younis, A., Noh, D., Thalassinos, K., Raleigh, D.P., (2020). Analysis of proline substitutions reveals the plasticity and sequence sensitivity of human IAPP amyloidogenicity and toxicity. *Biochemistry* **59** (6), 742–754.
31. Abedini, A., Raleigh, D.P., (2006). Destabilization of human IAPP amyloid fibrils by proline mutations outside of the putative amyloidogenic domain: is there a critical amyloidogenic domain in human IAPP?. *J. Mol. Biol.* **355** (2), 274–281.
32. Myriam M. Altamirano-Bustamante, Nelly F. Altamirano-Bustamante, Mateo Larralde-Laborde, Reyna Lara-Martínez, Edgar Leyva-García, Eulalia Garrido-Magaña, Gerardo Rojas, Luis Felipe Jiménez-García, Cristina Revilla-Monsalve, Perla Altamirano, et al. Unpacking the aggregation-oligomerization-fibrillization process of naturally-occurring hiapp amyloid oligomers isolated directly from sera of children with obesity or diabetes mellitus. Sci. Rep., 9(1):18465, 2019.
33. Xu, Y., Maya-Martinez, R., Guthertz, N., Heath, G.R., Manfield, I.W., Breeze, A.L., Sobott, F., Foster, R., Radford, S.E., (2022). Tuning the rate of aggregation of hIAPP into amyloid using small-molecule modulators of assembly. *Nat. Commun.* **13** (1), 1040.
34. Bortoletto, A.S., Graham, W.V., Trout, G., Bonito-Oliva, A., Kazmi, M.A., Gong, J., Weyburne, E., Houser, B.L., Sakmar, T.P., Parchem, R.J., (2022). Human Islet Amyloid Polypeptide (hIAPP) Protofibril-Specific Antibodies for Detection and Treatment of Type 2 Diabetes. *Adv. Sci.* **9** (34), 2202342.
35. Lövestam, S., Li, D., Wagstaff, J.L., Kotecha, A., Kimanius, D., McLaughlin, S.H., Murzin, A.G., Freund, S.M.V., Goedert, M., Scheres, S.H.W., (2024). Disease-specific tau filaments assemble via polymorphic intermediates. *Nature* **625** (7993), 119–125.
36. Xue, C., Lin, T.Y., Chang, D., Guo, Z., (2017). Thioflavin T as an amyloid dye: fibril quantification, optimal concentration and effect on aggregation. *R. Soc. Open Sci.* **4** (1), 160696.
37. Valli, D., Ooi, S.A., Scattolini, G., Chaudhary, H., Tietze, A. A., Maj, M., (2024). Improving cryo-EM grids for amyloid fibrils using interface-active solutions and spectator proteins. *Biophys. J.* **123** (6), 718–729.
38. Lau, A., So, R.W.L., Lau, H.H.C., Sang, J.C., Ruiz-Riquelme, A., Fleck, S.C., Stuart, E., Menon, S., Visanji, N.P., Meisl, G., Faidi, R., Marano, M.M., Schmitt-Ulms, C., Wang, Z., Fraser, P.E., Tandon, A., Hyman, B.T., Wille, H., Ingelsson, M., Klenerman, D., Watts, J.C., (2020). α-Synuclein strains target distinct brain regions and cell types. *Nat. Neurosci.* **23**, 21–31.

39. Sinnige, T., (2022). Molecular mechanisms of amyloid formation in living systems. *Chem. Sci.* **13** (24), 7080–7097.
40. Zapadka, K.L., Becher, F.J., Gomes dos Santos, A., Jackson, S.E., (2017). Factors affecting the physical stability (aggregation) of peptide therapeutics. *Interface Focus* **7** (6), 20170030.
41. Berardet, C., Kaffy, J., Halgand, F., Van der Rest, G., Ongeri, S., Taverna, M., (2020). Evidence for different in vitro oligomerization behaviors of synthetic hIAPP obtained from different sources. *Anal. Bioanal. Chem.* **412**, 3103–3111.
42. Fortin, J.S., Benoit-Biancamano, M.-O., (2015). Wildlife sequences of islet amyloid polypeptide (IAPP) identify critical species variants for fibrillization. *Amyloid* **22** (3), 194–202.
43. Valli, D., Ooi, S.A., Kaya, I., Thomassen, A.B., Chaudhary, H., Weidner, T., Andrén, P.E., Maj, M., (2025). Cryo-Electron Microscopy Provides Mechanistic Insights into Solution-Dependent Polymorphism and Cross-Aggregation Phenomena of the Human and Rat Islet Amyloid Polypeptides. *Biochemistry* **64** (12), 2583–2595.
44. Bepler, T., Morin, A., Rapp, M., Brasch, J., Shapiro, L., Noble, A.J., Berger, B., (2019). Positive-unlabeled convolutional neural networks for particle picking in cryo-electron micrographs. *Nat. Methods* **16** (11), 1153–1160.
45. Scheres, S.H., (2012). RELION: implementation of a Bayesian approach to cryo-EM structure determination. *J. Struct. Biol.* **180** (3), 519–530.
46. Kimanius, D., Dong, L., Sharov, G., Nakane, T., Scheres, S.H., (2021). New tools for automated cryo-EM single-particle analysis in RELION-4.0. *Biochem. J.* **478** (24), 4169–4185.
47. Bücker, Robert, Seuring, Carolin, Cazey, Cornelia, Veith, Katharina, García-Alai, Maria, Grünewald, Kay, Landau, Meytal, (2022). The cryo-em structures of two amphibian antimicrobial cross-β amyloid fibrils. *Nat. Commun.* **13** (1), 4356.
48. Hervas, R., Rau, M.J., Park, Y., Zhang, W., Murzin, A.G., Fitzpatrick, J.A., Scheres, S.H., Si, K., (2020). Cryo-EM structure of a neuronal functional amyloid implicated in memory persistence in Drosophila. *Science* **367** (6483), 1230–1234.
49. Seidler, P.M., Murray, K.A., Boyer, D.R., Ge, P., Sawaya, M.R., Hu, C.J., Cheng, X., Abskharon, R., Pan, H., DeTure, M.A., Williams, C.K., Dickson, D.W., Vinters, H.V., Eisenberg, D.S., (2022). Structure-based discovery of small molecules that disaggregate Alzheimer's disease tissue derived tau fibrils in vitro. *Nat. Commun.* **13** (1), 5451.
50. Goldschmidt, L., Teng, P.K., Riek, R., Eisenberg, D., (2010). Identifying the amylome, proteins capable of forming amyloid-like fibrils. *Proc. Natl. Acad. Sci. U.S.A.* **107** (8), 3487–3492.
51. Tenidis, K., Waldner, M., Bernhagen, J., Fischle, W., Bergmann, M., Weber, M., Merkle, M.-L., Voelter, W., Brunner, Kapurniotu, A., (2000). Identification of a penta- and hexapeptide of islet amyloid polypeptide (IAPP) with amyloidogenic and cytotoxic properties. *J. Mol. Biol.* **295** (4), 1055–1071.
52. Buchanan, L.E., Dunkelberger, E.B., Tran, H.Q., Cheng, P.-N., Chiu, C.-C., Cao, P., Raleigh, D.P., De Pablo, J.J., Nowick, J.S., Zanni, M.T., (2013). Mechanism of IAPP amyloid fibril formation involves an intermediate with a transient β-sheet. *Proc. Natl. Acad. Sci. U.S.A.* **110** (48), 19285–19290.
53. Serrano, A.L., Lomont, J.P., Tu, L.-H., Raleigh, D.P., Zanni, M.T., (2017). A free energy barrier caused by the refolding of an oligomeric intermediate controls the lag time of amyloid formation by hIAPP. *J. Am. Chem. Soc.* **139** (46), 16748–16758.
54. Sawaya, M.R., Hughes, M.P., Rodriguez, J.A., Riek, R., Eisenberg, D.S., (2021). The expanding amyloid family: Structure, stability, function, and pathogenesis. *Cell* **184** (19), 4857–4873.
55. Poyner, D.R., Sexton, P.M., Marshall, I., Smith, D.M., Quirion, R., Born, W., Muff, R., Fischer, J.A., and Foord, S. M. International Union of Pharmacology. XXXII. The mammalian calcitonin gene-related peptides, adrenomedullin, amylin, and calcitonin receptors. Pharmacol. Rev. 54(2), 233–246 (2002).
56. Hay, D.L., Pioszak, A.A., (2016). Receptor activity-modifying proteins (RAMPs): new insights and roles. *Annu. Rev. Pharmacol. Toxicol.* **56**, 469–487.
57. Cao, J., Belousoff, M.J., Liang, Y.-L., Johnson, R.M., Josephs, T.M., Fletcher, M.M., Christopoulos, A., Hay, D. L., Danev, R., Wootten, D., et al., (2022). A structural basis for amylin receptor phenotype. *Science* **375** (6587), eabm9609.
58. Marek, P., Woys, A.M., Sutton, K., Zanni, M.T., Raleigh, D. P., (2010). Efficient microwave-assisted synthesis of human islet amyloid polypeptide designed to facilitate the specific incorporation of labeled amino acids. *Org. Lett.* **12** (21), 4848–4851.
59. Zheng, S.Q., Palovcak, E., Armache, J.-P., Verba, K.A., Cheng, Y., Agard, D.A., (2017). MotionCor2: anisotropic correction of beam-induced motion for improved cryo-electron microscopy. *Nat. Methods* **14** (4), 331–332.
60. Rohou, A., Grigorieff, N., (2015). CTFFIND4: Fast and accurate defocus estimation from electron micrographs. *J. Struct. Biol.* **192** (2), 216–221.
61. Cao, H., Li, T., He, J., Huang, S., (2025). BPS2025 - EMReady2: a general model for improving cryo-EM and cryo-ET maps by heterogeneity-aware deep learning. *Biophys. J.* **124** (3), 625a.
62. Emsley, P., Lohkamp, B., Scott, W.G., Cowtan, K., (2010). Features and development of Coot. *Acta Crystallogr. D* **66** (4), 486–501.
63. Afonine, P.V., Poon, B.K., Read, R.J., Sobolev, O.V., Terwilliger, T.C., Urzhumtsev, A., Adams, P.D., (2018). Real-space refinement in PHENIX for cryo-EM and crystallography. *Acta Crystallogr. D* **74** (6), 531–544.